Journal of Materials Research and Technology 31 (2024) 1419–1429

Contents lists available at ScienceDirect

Journal of Materials Research and Technology

journal homepage: www.elsevier.com/locate/jmrt

# Tribocorrosion behaviour of additively manufactured β-type Ti–Nb alloy for implant applications

Adnan Akman [a,b,*], Yohan Douest [c,d], Ludovico Andrea Alberta [a], Kevin Perrin [d], Ana-Maria Trunfio Sfarghiu [e], Nicolas Courtois [c], Benoit Ter-Ovanessian [d], Stefan Pilz [a], Martina Zimmermann [b], Mariana Calin [a], Annett Gebert [a]

[a] Leibniz Institute for Solid State and Materials Research Dresden, Helmholtzstr. 20, D-01069, Dresden, Germany
[b] Institute of Materials Science, TU Dresden, Helmholtzstr. 7, 01069, Dresden, Germany
[c] Anthogyr SAS, F-74700, Sallanches, France
[d] Univ. Lyon, INSA de Lyon, MATEIS, UMR CNRS 5510, 69621, Villeurbanne, France
[e] Univ. Lyon, INSA de Lyon, LaMCoS, UMR CNRS 5259, 69621, Villeurbanne, France

ARTICLE INFO

Handling Editor: P.Y. Chen

*Keywords:*
β-titanium alloy
Tribocorrosion
Biomaterial
Laser powder bed fusion

ABSTRACT

β-type Ti–Nb alloys are promising materials for load-bearing implant applications with improved mechanical biofunctionality and biocompatibility. In this work, the electrochemical and tribo-electrochemical behaviour of laser powder bed fusion (LPBF) produced β-type Ti–42Nb alloy processed via Gaussian and top hat laser was investigated and compared with commercial grade β-type Ti–45Nb and α+β-type Ti–6Al–4V ELI. Electrochemical impedance spectroscopy (EIS) and potentiodynamic polarization experiments were performed in phosphate-buffered saline (PBS) for corrosion behaviour. Tribocorrosion behaviour was studied under open circuit potential (OCP) conditions in PBS by using a reciprocating pin-on-disk tribometer. The passivation nature of the LPBF alloys is more decisive than the microstructural particularities for electrochemical behaviour. The overall corrosion response is similar due to the protective nature of the passive films formed on Ti alloys. Ti–6Al–4V ELI exhibits the best corrosion performance among all tested alloys with lower corrosion and passivation current density values. However, LPBF-produced alloys exhibit less reactive surfaces with better passive film properties compared to Ti–45Nb. In addition, EIS results revealed that passive film resistance values are higher for LPBF-produced alloys than conventionally produced Ti–45Nb. LPBF-produced alloys exhibit better tribo-electrochemical behaviour compared to Ti–45Nb. The differences in volume loss are mainly attributed to the microhardness of the alloys and the volume loss is dominated by mechanical wear. The alloys produced with LPBF show promising corrosion and tribocorrosion performance to be a potential candidate for load-bearing implant applications.

## 1. Introduction

Titanium alloys have acquired a predominant position in the biomedical field for bone implant applications with mechanical biofunctionality and biocompatibility. However, commonly employed Ti alloys (cp-Ti, Ti–6Al–4V) in clinical use have Young's modulus values around 100–120 GPa, whereas reported Young's modulus values of bone are in the range of 4–30 GPa. For load-bearing implants, the mismatch in stiffness may cause stress-shielding effects leading to bone resorption [1,2]. In addition, Ti–6Al–4V alloy use has been questioned due to the presence of Al and V which are elements with a toxicity potential in certain chemical forms and conditions [3–5]. Therefore, β-type Ti alloys are the focus of current research for mainly two reasons; (i) excellent mechanical compatibility with appropriate strength, and (ii) absence of toxic alloying elements [6,7]. Among them, Ti–Nb-based alloys received significant attention for implant applications. Single-phase β-type

* Corresponding author. Leibniz Institute for Solid State and Materials Research Dresden, Helmholtzstr. 20, D-01069, Dresden, Germany.
*E-mail addresses:* a.akman@ifw-dresden.de (A. Akman), yohan.douest@anthogyr.com (Y. Douest), ludovico.alberta@hotmail.it (L.A. Alberta), kevin.perrin@insa-lyon.fr (K. Perrin), ana-maria.sfarghiu@insa-lyon.fr (A.-M. Trunfio Sfarghiu), nicolas.courtois@anthogyr.com (N. Courtois), benoit.ter-ovanessian@insa-lyon.fr (B. Ter-Ovanessian), s.pilz@ifw-dresden.de (S. Pilz), martina.zimmermann@tu-dresden.de (M. Zimmermann), m.calin@ifw-dresden.de (M. Calin), a.gebert@ifw-dresden.de (A. Gebert).

https://doi.org/10.1016/j.jmrt.2024.06.172
Received 23 April 2024; Received in revised form 11 June 2024; Accepted 24 June 2024
Available online 25 June 2024

homogenized Ti–Nb alloys with 40–45 wt% Nb exhibits a low Young's modulus in the range of 63–70 GPa [8–10]. Material strengthening without substantially increasing Young's modulus values can be achieved by thermomechanical processing [10,11]. In addition, Ti–Nb alloys exhibit excellent corrosion behaviour with very low metal ion release rates owing to their strong passivation ability [12–15]. Their high Nb content and appropriate surface nano-roughening yield superior cytocompatibility [14,16,17].

Additive manufacturing techniques like laser powder bed fusion (LPBF) have received growing interest in medical engineering due to their ability to fabricate patient-specific implants in a layer-wise way with customized requirements and complex geometries [18–22]. However, the research activities are focused on commercial implant materials [23,24]. Limited studies are available regarding LPBF-produced β-type Ti–Nb alloys [25–30].

LPBF-produced β-type Ti–Nb alloys exhibit superior mechanical properties as compared to counterparts produced with traditional manufacturing methods due to their unique microstructures (due to high cooling rates during the LPBF process) [30,31]. Additionally, LPBF offers the opportunity to control the mechanical properties of the components by applying different processing parameters (i.e., laser speed, laser power, etc.). With this approach, implant materials can be locally adapted to the human bone [32–34]. Most of the LPBF devices are equipped with a laser with a Gaussian intensity distribution (beam diameter is less than 100 μm) [35]. However, this configuration shows two primary limitations. Firstly, they are prone to vapour-induced instabilities leading to the ejection of spatters. Secondly, their ability to increase the build-up rate is constrained by process instabilities. Thus, laser sources with an increased spot size are an alternative to Gaussian laser configurations to enhance process stability and increase the build-up rate [30,35].

Recently, Pilz et al. [30] studied the use of a top hat laser to produce β-type Ti–42Nb bulk samples with a strong texture, and the mechanical properties were compared with the same alloy composition (Ti–42Nb) produced with a Gaussian laser configuration. In the end, highly elongated grains with a {001} texture parallel to the building direction (BD) were generated by utilizing a top hat laser configuration. A Young's modulus ($E$) of 44 GPa was obtained parallel to the BD and 52 GPa was reached perpendicular to the BD via top hat laser configuration, which is lower than the Gaussian ones ($E = 67$–$69$ GPa), and the ones reported for LPBF-produced Ti–42Nb (e.g., $E = 62$ GPa [29,31,36]). In addition, the LPBF-produced samples exhibited superior yield strength compared to conventionally produced Ti–45Nb alloys [15]. The alloy samples produced with Gaussian laser exhibit yield strength values of 718 MPa (perpendicular to BD) to 742 MPa (parallel to BD). This slight difference between the yield strength values represents the isotropic behaviour of the studied alloys produced via Gaussian laser configuration. On the other hand, the alloy states produced with the top hat laser exhibited yield strength values of 690 MPa (perpendicular to BD) to 674 MPa (parallel to BD). The effect of the anisotropic nature (via top hat laser) is less pronounced in terms of yielding behaviour compared to Young's modulus. Therefore, by using a top hat laser configuration, Young's modulus values can be lowered significantly without lowering the yield strength to the same extent. The obtained results are quite promising for LPBF-produced β-type Ti–42Nb alloys. This approach enables the production of patient-specific implants with desired mechanical properties to control the stress-shielding effect. However, in-depth studies are needed to clarify the impact of LPBF-related microstructural states of those β-type Ti–42Nb alloys on other implant-relevant aspects, such as corrosion, wear, and tribocorrosion.

Implants are in contact with soft and hard tissues and body fluids. In addition, load-bearing implants are mostly subjected to relative movements (prosthesis and the surrounding bone) in the human body. Thus, it is essential to analyse interactions between mechanical loading and electrochemical reactions such as the tribocorrosion process for newly developed hard-tissue implant materials [37]. Under tribocorrosion conditions, the deterioration might be severe due to the combined effect of mechanical wear and corrosion [38–40]. In addition, due to this deterioration metal ion release can be accelerated, which may induce cytotoxicity [41–43].

Concerning corrosion and tribocorrosion behaviour, only a few studies are available for LPBF-produced β-type Ti alloys. Pede et al. [44] studied the corrosion performance of LPBF-produced β-type Ti–42Nb and Ti–20Nb–6Ta (wt.%) alloys in 0.9 wt% NaCl solution and compared it with that of conventionally manufactured α-type cp-Ti and α+β-type Ti–6Al–4V ELI alloys. Results revealed that LPBF-produced β-type Ti alloys exhibit superior corrosion performance due to the formation of a more protective oxide layer due to the contribution of Ta-based and/or Nb-based oxides to the growth of Ti-based oxides. Hariharan and Goldberg et al. [45] investigated the corrosion behaviour in PBS solution of near β-type Ti–13Nb–13Zr (wt.%) alloy samples in various microstructural states. All sample states (i.e., wrought and additively manufactured with different heat treatments) showed low free corrosion activity and stable anodic passivity. Qin et al. [46] studied the corrosion behaviour of LPBF-produced β-type Ti–35Nb (wt.%) in Hank's solution using mixed and pre-alloyed powder as a powder source. Results revealed that the alloy produced with pre-alloyed powder exhibits better corrosion performance than the alloy produced with mixed powder due to the formation of stable oxide films with a less defective nature. Additionally, due to the unmelted Nb particles, the passive film of the alloys produced with mixed powder exhibits a more defective nature. Limited information is available in the literature on the tribocorrosion behaviour of LPBF-produced Ti–Nb alloys. Chakkravarthy et al. [47] investigated the bio-tribocorrosion behaviour of an LPBF-produced near β-type Ti–25Nb (wt.%) alloy by comparing them with conventionally manufactured Ti–6Al–4V in acidic sodium lactate electrolyte. The results show that LPBF-fabricated Ti–25Nb alloy exhibits superior wear resistance due to its strong passivation nature, which attenuates contact shear stress during sliding, compared to commercial Ti–6Al–4V implant alloy. In addition, the poor tribological response of conventionally produced Ti–6Al–4V might be attributed to the lack of residual stresses due to the production process compared to the LPBF method, where high compressive residual stresses offer greater wear resistance.

The originality of the present work lies in reporting the tribocorrosion behaviour of LPBF-produced β-type Ti–42Nb alloy produced via Gaussian and high-power top hat laser configurations, alongside conventionally produced β-type Ti–45Nb and α+β-type Ti–6Al–4V ELI alloys. The effect of process-dependent microstructural particularities on the tribo-electrochemical behaviour was investigated. The present work is essential for assessing prospective candidates for the development of next-generation materials used in hard-tissue implants.

## 2. Experimental

### 2.1. Preparation of the alloy, microstructural, and mechanical characterization

Pre-alloyed, gas-atomized Ti–42Nb (wt.%) powder was supplied by TANIOBIS GmbH with a particle size in the range of 10–63 μm. Two different sample states of LPBF-produced Ti–42Nb (wt.%) with single β-phase microstructures [30,31] were investigated in this work. One set was processed using a Gaussian laser source, while the other was processed using a top hat laser source. Samples produced with the Gaussian laser, featuring a beam size of approximately 80 μm, were processed at a scanning speed of 1000 mm/s, a laser power of 250 W, a layer thickness of 50 μm, and a hatching distance of 100 μm. Conversely, for samples produced with the top hat laser, which features a larger beam size of around 680 μm, a higher laser power of 950 W was employed. Processing parameters include a laser scanning speed of 250 mm/s, a layer thickness of 100 μm, and a hatching distance of 500 μm. For both sample types, a stripe pattern with a vector rotation of 67° was applied. The process parameters (laser power, scanning speed, and hatching distance)

were optimized to achieve a high relative density (>99%). After the production, cylindrical alloy samples were cut perpendicular to the building direction (BD) with a diameter of 7 mm and thickness of 3 mm by electrical discharge machining. Comprehensive information about the alloy preparation is provided elsewhere [30,31]. Ti–45Nb (99.9%, ASTM B348-13) in the solution-treated state (at 1000 °C for 24 h) [15] and Ti–6Al–4V ELI (ASTM F136 grade 23, provided by Anthogyr SAS, France) in the as-received state were used as reference alloys. For microstructural studies, the samples were ground using SiC emery paper. For the polishing, a mixture of colloidal $SiO_2$ (90 vol%) and $H_2O_2$ (10 vol%) was used. The microstructure of the LPBF-produced alloys was studied by scanning electron microscopy (SEM; Leo Gemini 1530, Zeiss AG) equipped with an energy-dispersive X-ray spectrometer (EDX; XFlash 6|60, Bruker GmbH) and an electron backscatter diffraction (EBSD) detector (eFlash$^{HR}$, Bruker GmbH). The open-source toolbox MTEX (v.5.10.2) [48] was employed to assess the EBSD measurements and conduct texture analysis. To examine the phase composition of the samples, synchrotron X-ray diffraction (SXRD) was conducted at the High Energy Materials Science (HEMS) beamline [49] at PETRA III (Deutsches Elekronen-Synchrotron, DESY). Vickers microhardness ($HV_{0.1}$) was measured with a Falcon 600 indenter on polished samples by applying a 0.98 N load (10 s dwell time). The average hardness values with standard deviations are the result of 10 consecutive hardness measurements.

### 2.2. Chemical composition analysis

The elemental composition of the LPBF-produced alloys (Gaussian and top hat) was checked by inductively coupled plasma optical emission spectroscopy (iCAP 6500 Duo View, Thermo Fisher Scientific GmbH).

### 2.3. Corrosion tests

Electrochemical tests were performed in a phosphate-buffered saline (PBS) solution (NaCl 140 mM, KCl 3 mM, phosphate buffer 10 mM with a pH of 7.4, Merck KGaA) at room temperature to investigate the corrosion properties. For this purpose, the alloys were ground with SiC emery paper (down to P1200) and cleaned with ethanol. The samples were electrically connected with copper tape for electrochemical measurements.

For corrosion studies, a Solartron XM ModuLab potentiostat was used in combination with a three-electrode Teflon cell. The Ti alloys were used as the working electrode (the effective working electrode area is 0.385 $cm^2$). For LPBF-produced alloys, sample surfaces perpendicular to the building direction (BD) were used as a working electrode. As an auxiliary electrode, a platinum wire was used and the potentials were measured versus the silver chloride reference electrode (Ag/AgCl (E(Ag/AgCl) = 0.197 V vs. SHE). To determine the free corrosion response of the studied alloys, the open circuit potential (OCP) transient was monitored for 30 min. Then, potentiodynamic polarization experiments were conducted in a potential range between −0.3 V (vs. OCP) to 1 V (vs. Ag/AgCl) at a scan rate of 0.5 mV/s. ECLab software (v11.36) was used for Tafel extrapolation (Tafel's approximation only applies when there is charge transfer. For passivated material, the current is not limited by charge transfer. Thus, passive metals are not usually compared based on their corrosion current). For further investigation, electrochemical impedance spectroscopy (EIS) studies were carried out after 90 min of OCP stabilization. EIS measurements were conducted in the frequency range from 10 kHz to 0.01 Hz by applying a perturbation amplitude of 10 mV. Zview 4 software was used for analysing the EIS data. The experiments were performed three times to ensure data reproducibility.

### 2.4. Tribocorrosion tests

Tribocorrosion tests were performed at room temperature in PBS solution using a pin-on-disk tribometer under a reciprocating sliding configuration. A Gamry potentiostat (Reference-600) was employed with a three-electrode cell setup. Schematic representation and pictures of the setup were presented elsewhere [50]. For the tribocorrosion experiments, the Ti alloys were used as the working electrode against an alumina ball (6 mm in diameter, a curvature radius of 26 mm [50]), a platinum wire was used as the counter electrode, and a saturated silver chloride electrode (Ag/AgCl) was employed as the reference electrode. The pin was polished before the experiments with SiC emery paper (grit size P4000) to maintain the same radius of curvature to get reproducible results. The tribocorrosion tests were performed under a reciprocating sliding frequency of 0.5 Hz for 30 min with a sliding displacement of around 2 mm. The applied load was fixed to 4 N during the sliding. The shear forces during sliding were recorded with a tribometer and coefficient of friction (COF) values were calculated from the ratio between shear and normal forces. Hertzian contact pressures (maximum) [51] were calculated as 0.17, 0.17, and 0.21 GPa for Ti–45Nb, Gaussian (LPBF-produced), and Ti–6Al–4V ELI alloys, respectively. Due to the anisotropic nature (in terms of mechanical properties) of the Ti–42Nb alloys (LPBF alloy) produced with the top hat laser configuration, Poisson's ratios were not calculated. Thus, the Hertzian contact pressures were not included in this work.

The tribocorrosion tests were performed under open circuit potential (OCP) conditions, where the potential of the studied alloy samples is controlled by the tribological parameters and the physicochemical properties of the environment. The experimental procedure consisted of the monitoring of the OCP for 30 min without sliding, at which a steady state was achieved, and then subsequently sliding for 30 min to reveal the tribocorrosion response of the studied alloys under free corrosion conditions. In the end, sliding was stopped after 30 min, and OCP was measured for 30 min to complete the experiment. The tribocorrosion experiments were repeated twice for reproducibility assessment.

### 2.5. Characterization of wear tracks

Worn areas were analysed by a combination of scanning electron microscopy (SEM) and 3D confocal profilometry. A Zeiss Leo Gemini 1530 SEM was used under an accelerating voltage of 20 kV. The total volume loss ($V_{tot}$), wear depth ($D$), and total wear area of the worn areas were investigated with an S Neox 3D confocal profilometer (non-contact) in a confocal mode. The areas of interest (worn areas) were analysed by the *Sensomap standard* (v. 6.7) software.

### 2.6. Metal ion release after tribocorrosion

An inductively coupled plasma-mass spectrometry (ICP-MS) was employed for ion release studies. The solutions from the tribocorrosion experiments were stored in plastic containers. For the analyses, the samples were diluted in $HNO_3$ solution (100 μL in 10 mL total volume). The metal ions analysed were Ti-48 and Nb-93, which had detection limits of 7.4 ppt and 3.8 ppt, respectively. Fresh PBS was also measured as the blank solution, and tests were repeated twice.

## 3. Results

### 3.1. Microstructural properties and microhardness

For the planned corrosion and tribocorrosion analyses, two series of Ti–42Nb samples were fabricated using the laser powder bed fusion (LPBF) process, utilizing a Gaussian laser source for one series and a top hat laser source for the other [30,31]. The chemical composition of the samples is provided in Table 1. A single β-type microstructure was observed for both sample types through SXRD analysis (see Supplementary Fig. 1). To examine the microstructure of the LPBF-produced samples, SEM and EBSD analyses were performed on surfaces perpendicular to the building direction (X–Y plane), depicted in Fig. 1. These

**Table 1**
Measured chemical composition of the LPBF-produced alloys (in wt.%).

| Alloys (Ti–42Nb wt. %) | Ti | Nb | O | N |
|---|---|---|---|---|
| **Gaussian laser** | 58.06 ± 0.91 | 41.79 ± 0.39 | 0.291 ± 0.005 | 0.016 ± 0.004 |
| **Top hat laser** | 57.76 ± 0.57 | 41.92 ± 0.23 | 0.294 ± 0.002 | 0.018 ± 0.006 |

surfaces corresponded to the sample planes used for the subsequent corrosion and tribocorrosion analysis.

The EBSD maps in Fig. 1b and d illustrate the crystal orientation alongside with grain boundaries (≥15°) in black and sub-grain boundaries (3°–15°) in grey. For the samples produced with the Gaussian laser, the applied laser scan paths are discernible, and the grain morphology displays a significant variation, ranging from square-shaped or circular grains to highly elongated ones or circular grains to highly elongated ones. Moreover, subgrain boundaries are visible in some grains. The crystal orientations relative to the surface plane do not exhibit any preferred orientation and the inverse pole figures (IPF) of the sample (Supplementary Fig. 2) illustrate a nearly isotropic distribution of the crystal orientations along the 3 principal axes.

In contrast, a completely different microstructure is observed for samples obtained with the top hat laser configuration. The oriented heat flow towards the substrate plate favour the columnar growth of grains parallel to the BD. This results in a pronounced {001} texture parallel to the building direction, as observed in the orientation map in Fig. 1d and the IPFs in Supplementary Fig. 2. The grain boundaries exhibit a more irregular profile and a high amount of subgrain boundaries are evident in the microstructure.

For both sample series, the average grain size was determined using a line intersection method, measuring the chord length distribution for the microstructure at various angles. For samples, produced with the Gaussian laser, a mean chord length of 18.7 μm was determined, with a variation from 17.0 μm to 21.6 μm for the different measurement angles. These values are consistent with earlier analysis of the same sample type [31]. In contrast, for the top hat laser samples, the grain size and the mean chord length are significantly increased to 100.7 μm, with only a small variation from 93.8 μm to 103.5 μm for the different measurement angles. On the other hand, for conventionally produced alloys, equiaxed β-grains and biphasic (α+β) microstructure with elongated grains were observed for β-type Ti–45Nb and α+β-type Ti–6Al–4V ELI, respectively. More details about the microstructural properties of these conventional alloys can be found elsewhere [15,50].

SEM images for both sample types (Fig. 1a and c and Fig. 2a and c) reveal a cellular/cellular-dendritic solidification structure, typical for LPBF-processed β-type Ti–Nb alloys [27,30,52]. As the size of the solidification cells is related to the applied cooling rate (the solidification rate is higher for Gaussian laser configuration than top hat one), significantly smaller cells are observed for the Gaussian samples (around 0.5–2 μm) when compared to the top hat ones (approximately 3–5 μm). In both cases, coarser cells are found near the melt pool boundaries and the cellular structure exhibits Nb-rich (Ti-lean) cellular regions and Nb-lean (Ti-rich) intercellular regions. These compositional variations are depicted in Fig. 2 by EDX (elemental mappings) and result from non-equilibrium partitioning during the rapid solidification, inherent to the LPBF process [53]. Further information about the microstructural features of the alloys has been provided previously [30,31].

Vickers microhardness ($HV_{0.1}$) values are 155 ± 4 $HV_{0.1}$ *and* 348 ± 5 $HV_{0.1}$ for Ti–45Nb and Ti–6Al–4V ELI, respectively. For the alloy samples produced via Gaussian and top hat laser configuration, hardness values are measured as 226 ± 6 $HV_{0.1}$ and 230 ± 2 $HV_{0.1}$, respectively. Due to the high solidification and cooling rates, LPBF-produced Ti–42Nb alloys with cellular structures exhibit high hardness compared to Ti–45Nb alloys (155 ± 4 $HV_{0.1}$). In addition, the difference in hardness values is attributed to the oxygen content as an interstitial element in the LPBF-produced Ti alloys. In some works [54–57], oxygen addition has been considered an effective strategy to improve the strength of the Ti alloys via solid solution strengthening. Due to the high content of

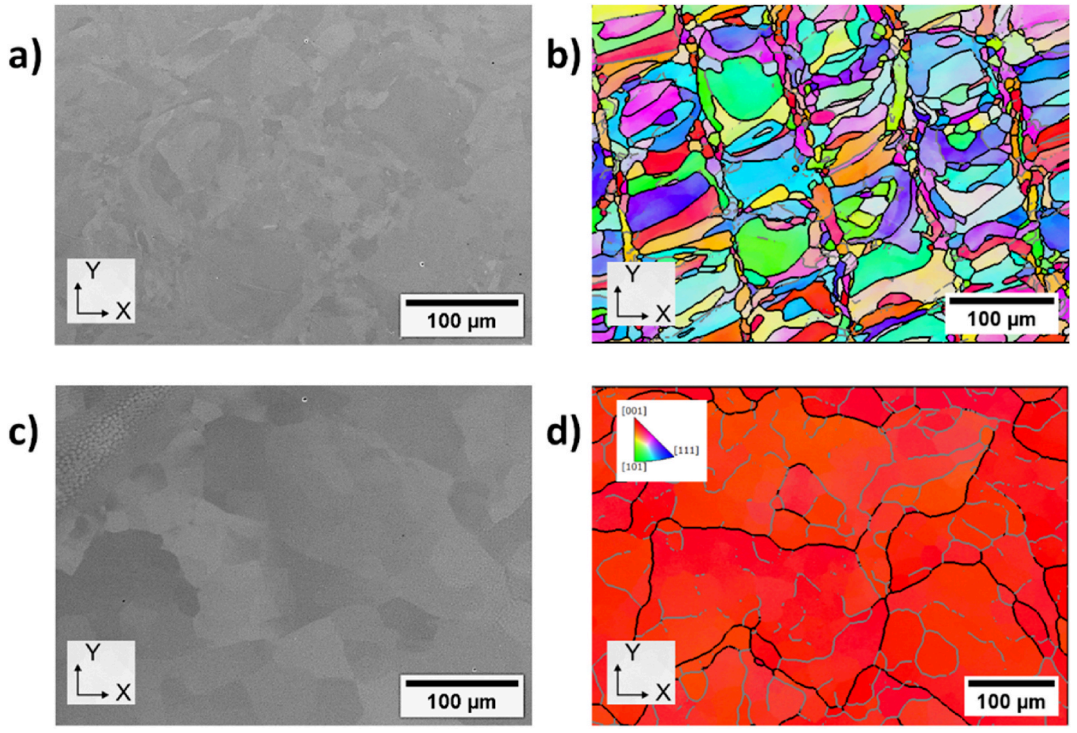


**Fig. 1.** Scanning electron microscopy (SEM) and inverse pole figure (IPF) mappings of LPBF-produced Ti–42Nb alloy samples produced with a Gaussian (a & b) and top hat (c & d) configuration. The IPF colour coding is given for the sample surface. Grain boundaries (≥15°) are marked with black and sub-grain boundaries (3°–15°) with grey lines. (For interpretation of the references to colour in this figure legend, the reader is referred to the Web version of this article.)

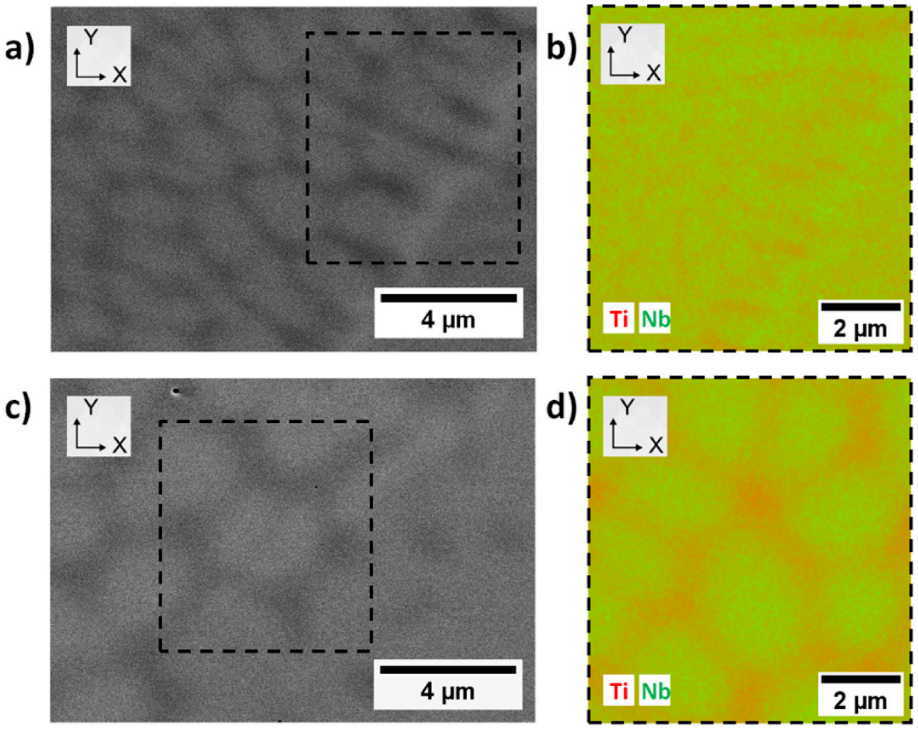


**Fig. 2.** Secondary electron (SE) images (a & c) and corresponding Energy Dispersive X-ray (EDX) maps (b & d) of LPBF-produced Ti–42Nb alloys fabricated using Gaussian (a & b) and top hat laser (c & d) configurations. Spectra were recorded at 5 keV to enhance lateral resolution and Ti-L and Nb-L X-ray lines were used for analysis.

oxygen in LPBF-produced alloys (0.291 wt% and 0.294 wt% for Gaussian and top hat laser, respectively) compared to conventionally produced Ti–45Nb (0.09 wt%) [50], LPBF-produced alloys show higher hardness values compared to Ti–45Nb.

In addition for the LPBF process, the generation of residual stresses is unavoidable due to rapid solidification rates [30,31]. The formation of residual stresses can be either tensile or compressive. Tensile residual stresses are not desirable due to the formation of stress corrosion cracking or fatigue damage. However, the formation of compressive residual stresses promotes greater wear resistance [47]. In our case, the solidification rate for the Gaussian laser is higher than the top hat one. Thus, the alloys produced with a Gaussian laser configuration might generate more compressive residual stress accumulation due to the high cooling rates.

### 3.2. Corrosion tests

Conventional electrochemical tests were performed to reveal the corrosion behaviour of the different alloy samples in PBS solution. Initially, the open circuit potential (OCP) was monitored for 30 min to achieve a steady state. Then, potentiodynamic polarization experiments were conducted. The potentiodynamic polarization curves are shown in Fig. 3 and calculated corrosion potential ($E_{corr}$), corrosion current density ($i_{corr}$), and passivation current density ($i_{pass}$) values from the polarization curves are given in Table 2. $E_{corr}$ values of the studied alloys are in a narrow range between −0.258 ÷ −0.203 V vs. Ag/AgCl and all tested alloys exhibit low $i_{corr}$ values in the range of 0.22 ÷ 0.53 μA/cm$^2$. However, Ti–6Al–4V ELI exhibits lower corrosion current densities compared to the rest of the studied alloys. The anodic branch of the potentiodynamic polarization curves shows in all cases a stable passive region until 1 V vs. Ag/AgCl with no passivity breakdown. This is due to the formation of very stable barrier-type oxide films, which is common for β-type Ti–Nb alloys and similar to cp-Ti and Ti–6Al–4V [58,59]. However, slight differences can be observed in the $i_{pass}$ values, e.g. by comparing values at 0.4 V vs. Ag/AgCl, which are given in Table 2. The

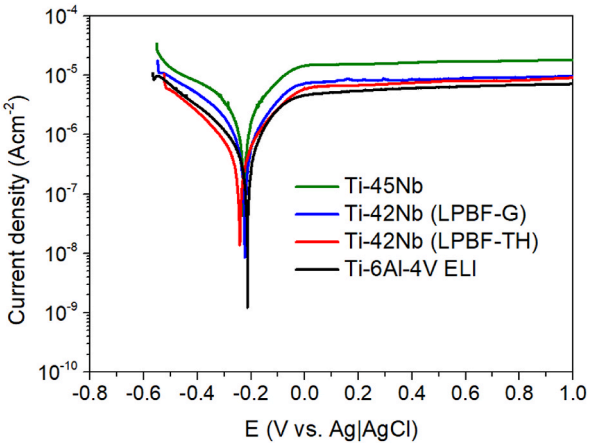


**Fig. 3.** Potentiodynamic polarization curves of Ti–45Nb, Ti–42Nb (LPBF-Gaussian laser), Ti–42Nb (LPBF-top hat laser), and Ti–6Al–4V ELI alloys in PBS solution after 30 min of OCP stabilization.

**Table 2**
Corrosion potential ($E_{corr}$), corrosion current density ($i_{corr}$), and passivation current density ($i_{pass}$) (at 0.4 V (vs. Ag/AgCl)) values were obtained for Ti–45Nb, Ti–42Nb (LPBF-Gaussian laser), Ti–42Nb (LPBF-top hat laser), and Ti–6Al–4V ELI alloy states from potentiodynamic polarization experiments.

| | $E_{corr}$ (V vs. Ag/AgCl) | $i_{corr}$ (μA/cm$^2$) | $i_{pass}$ (μA/cm$^2$) |
|---|---|---|---|
| **Ti–45Nb** | −0.218 ± 0.005 | 0.52 ± 0.12 | 15.5 ± 0.9 |
| **Ti–42Nb (LPBF-G)** | −0.258 ± 0.035 | 0.53 ± 0.05 | 8.5 ± 0.1 |
| **Ti–42Nb (LPBF-TH)** | −0.231 ± 0.018 | 0.35 ± 0.10 | 8.9 ± 1.2 |
| **Ti–6Al–4V ELI** | −0.203 ± 0.018 | 0.22 ± 0.10 | 5.2 ± 0.8 |

$i_{pass}$ values for the two LPBF-produced alloy states are similar and, they are lower compared to commercial Ti–45Nb. This reveals that the passive films formed on Ti–45Nb alloy has more reactive nature than the LPBF-produced alloys. Further, commercial Ti–6Al–4V ELI exhibits the best corrosion performance among all tested alloys with lower corrosion and passivation current density values. For a detailed analysis of the passive films, electrochemical impedance spectroscopy (EIS) measurements were performed.

Electrochemical impedance spectroscopy (EIS) is used to evaluate the properties of the passive films formed under OCP conditions in PBS solution. Fig. 4a shows representative Nyquist plots with the equivalent electrical circuit (EEC) and Fig. 4b shows representative Bode plots for the studied alloys. In the EEC, $R_1$ represents the solution resistance, $R_2$ and $CPE_1$ are related to the resistive and capacitive responses of the passive film grown under OCP for 90 min, respectively. A constant phase element (CPE) instead of an ideal capacitor is used [46,60–63]. The deviation from the ideal capacitive response can be attributed to the heterogeneities and defects in the passive film. The regressed resistance and capacitance values after the EEC fitting are reported in Table 3. The experimental data is in agreement with the EEC fitting due to the low chi-square ($\chi^2 < 0.01$) values.

In principle, the higher the impedance of the passive film, the larger the Nyquist arc radius [64]. All alloy samples behaved similarly during the measurements in terms of the shape of the arc. However, the arc radius is slightly larger for LPBF-produced alloy samples compared to Ti–45Nb, as depicted in Fig. 4a. In addition, for the Bode plots (Fig. 4b), the high-frequency range (phase angle drops to values near zero between $10^4$ Hz to $10^3$ Hz) represents the electrolyte resistance. At the intermediate frequency range ($10^3$ Hz–$10^0$ Hz), the phase angle values rise. At low frequencies ($10^0$ Hz to $10^{-2}$ Hz), the phase angle plot decreases to lower values which represents the passive film resistance [65]. The Bode impedance values (|Z|) are higher for LPBF-produced alloys (76.6 ± 6.1 kΩcm$^2$ and 85.5 ± 13.1 kΩcm$^2$ for Gaussian and top hat laser configurations, respectively) compared to Ti–45Nb (65.9 ± 13.3 kΩcm$^2$) at the lowest frequency of $10^{-2}$ Hz. LPBF-produced alloys with higher film resistance ($R_2$) values exhibit better passive film behaviour with a more protective nature compared to Ti–45Nb alloys as seen in Table 3. However, no significant difference was found between the two LPBF-produced alloy states. Ti–6Al–4V ELI exhibits better passive film properties with higher film resistance (2.50 ± 0.42 Ωcm$^2$x10$^5$) and bode impedance values (166.7 ± 2.5 kΩcm$^2$) compared to the rest of the studied alloy samples. LPBF-produced alloys exhibit lower capacitance ($CPE_1$-$Q$) and higher film resistance ($R_2$) values compared to Ti–45Nb, as seen in Table 3. In addition, the effective capacitance ($C_{eff}$) values can be calculated from the derived Burg's equation by using the passive film resistance ($R_2$) and CPE values ($CPE_1$-$Q$ and $CPE_1$-$n$) [66]. The passive film thickness can be estimated from the calculated effective capacitance ($C_{eff}$) values [64,67]. In our case, it is possible to expect similar passive film thickness under OCP conditions for Ti–Nb alloys due to their similar passivation nature. Also, *CPE1-n* values of all alloys showed similar capacitive behaviour of around 0.88, which means that the electrochemical response of the oxide film formed under free corrosion conditions slightly deviates from the pure capacitive behaviour due to the presence of heterogeneities/defects in the passive film. EIS results match well with the potentiodynamic polarization results. As discussed before, Ti–45Nb alloys with higher passivation current densities ($i_{pass}$) and lower passive film resistance ($R_2$) values exhibit more reactive surfaces than the LPBF-produced alloys. However, no significant difference was found between the two LPBF-produced alloy states. The differences in microstructural states for Gaussian and top-hat laser configurations do not yield a difference in the electrochemical behaviour. This is attributed to the similar and strong passivation nature of LPBF-produced alloys due to the major contribution of Ti and Nb to passivation (Nb species are involved in the oxidation processes by forming Ti–Nb mixed oxide) [13,58,68].

**Table 3**
The fitting values of the electrical equivalent circuit (EEC) components applied to EIS spectra of Ti–45Nb, Ti–42Nb (LPBF-Gaussian laser), Ti–42Nb (LPBF-top hat laser), and Ti–6Al–4V ELI alloys.

| | $R_1$ (Ωcm$^2$) | $R_2$ (Ωcm$^2$x10$^5$) | $CPE_1$-$Q$ (Ω$^{-1}$s$^n$cm$^2$x10$^{-5}$) | $CPE_1$-n |
|---|---|---|---|---|
| **Ti–45Nb** | 30 ± 1 | 0.95 ± 0.18 | 11.3 ± 1.5 | 0.88 ± 0.02 |
| **Ti–42Nb (LPBF-G)** | 32 ± 4 | 1.36 ± 0.15 | 5.6 ± 0.9 | 0.89 ± 0.03 |
| **Ti–42Nb (LPBF-TH)** | 30 ± 2 | 1.48 ± 0.32 | 6.5 ± 2.2 | 0.88 ± 0.01 |
| **Ti–6Al–4V ELI** | 29 ± 1 | 2.50 ± 0.42 | 4.3 ± 0.7 | 0.87 ± 0.01 |

### 3.3. Tribocorrosion tests

The tribocorrosion performance of the alloys was studied in PBS solution at room temperature. The evolution of the open circuit potential (OCP) values before, during, and after sliding together with the coefficient of friction (COF) values was monitored. The recorded potential values during tribocorrosion experiments represent the potential of the whole working electrode area. The potential change over time for

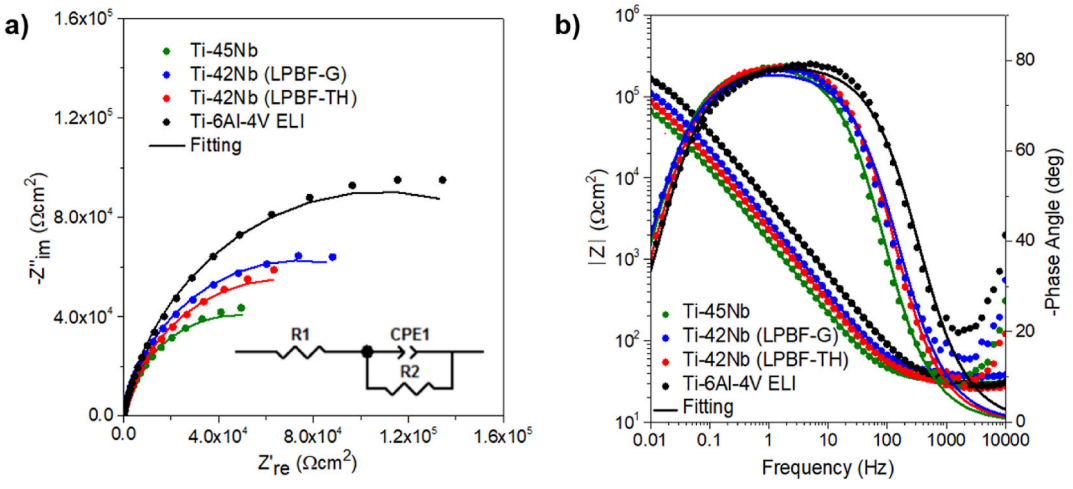


**Fig. 4.** EIS measurements - a) Nyquist plot and b) Bode plot of Ti–45Nb, Ti–42Nb (LPBF-Gaussian laser), Ti–42Nb (LPBF-top hat laser), and Ti–6Al–4V ELI alloys with the equivalent electrical circuit (EEC) used to interpret the EIS data. Before EIS measurements, samples were OCP stabilized for 90 min in PBS solution.

the studied alloys with COF values is illustrated in Fig. 5. Before the sliding starts (t = 1800 s), the potential reflects the formation of a passive film on the surface of the studied alloy samples. A sudden potential drop is observed after the initiation of the sliding. This potential decrease represents the local breakdown of the passive film (depassivation) due to the damage caused by the sliding action of the pin. The change in the potential in the worn area (depassivated region) during sliding raises the chances for the formation of galvanic coupling between the depassivated region (anodic worn area) and the neighbouring passive regions (cathodic unworn area) [69]. During sliding, the OCP remains practically constant, which is attributed to the dynamic equilibrium between depassivation and repassivation. After sliding (t = 3600 s), the potential values increased rapidly nearly to the pre-sliding values. The phenomenon is known as repassivation.

The potentials during tribocorrosion experiments are listed in Table 4. In addition, the potential drop ($|\Delta E|$) was calculated from the initial potential drop of sliding. The OCP curves of the studied alloys exhibit similar trends before, during, and after sliding. However, the lowest potential drop during the onset of sliding was detected for Ti–6Al–4V ELI ($|\Delta E| = 0.338$ V). However, within the error limits of the method, no significant difference was found between LPBF-produced alloys, i.e. ($|\Delta E| = 0.487$ V and $|\Delta E| = 0.505$ V were obtained for alloys produced with Gaussian and top hat laser configurations, respectively). This is similar to the mean value for Ti–45Nb with $|\Delta E| = 0.478$ V. The potential curves of the studied alloys become noisier during sliding due to cyclic depassivation and repassivation of the passive film. The curve belonging to Ti–6Al–4V ELI is slightly noisier than those of LPBF-produced alloy samples and commercial Ti–45Nb (Fig. 5c). The variation in potential is observed in the case of Ti–6Al–4V ELI ranging between – 0.752 and – 0.664 V vs. Ag/AgCl (in the range of ~0.08 V).

**Table 4**
Electrochemical parameters were obtained from the OCP curves before, during, and after sliding for Ti–45Nb, Ti–42Nb (LPBF-Gaussian laser), Ti–42Nb (LPBF-top hat laser), and Ti–6Al–4V ELI alloys. Potential values are reported vs. Ag/AgCl (E(Ag/AgCl) = 0.197 V vs. SHE).

| | Potential before sliding $E_{OCP}^{start}$ | Potential during sliding $E_{OCP}^{sliding}$ | Potential after sliding $E_{OCP}^{end}$ | Potential drop $\|\Delta E\|$ |
|---|---|---|---|---|
| **Ti–45Nb** | −0.248 ± 0.018 | −0.750 ± 0.002 | −0.241 ± 0.065 | 0.478 ± 0.075 |
| **Ti–42Nb (LPBF-G)** | −0.198 ± 0.053 | −0.705 ± 0.096 | −0.251 ± 0.054 | 0.487 ± 0.018 |
| **Ti–42Nb (LPBF-TH)** | −0.153 ± 0.010 | −0.700 ± 0.080 | −0.185 ± 0.007 | 0.505 ± 0.082 |
| **Ti–6Al–4V ELI** | −0.280 ± 0.017 | −0.721 ± 0.037 | −0.228 ± 0.025 | 0.338 ± 0.020 |

However, the rest of the studied alloys exhibit more steady-state potential change during sliding, in the range of ~0.05 V, which means that LPBF-produced alloys and Ti–45Nb reach dynamic equilibrium slightly faster than Ti–6Al–4V ELI. A similar observation for the potential fluctuations was made by different authors for conventionally produced Ti–6Al–4V [50,70] and Ti–45Nb [50]. In the final period of the tribocorrosion experiments, i.e., after sliding, the potential of all studied alloys increases rapidly due to the re-formation of a new passive film on the sliding regions. To evaluate the tribocorrosion behaviour of the LPBF-produced alloys further, the repassivation rate after sliding for a certain period was calculated according to the following equation [71]:

$$\Delta E = k_1 \log t + k_2 \quad (1)$$

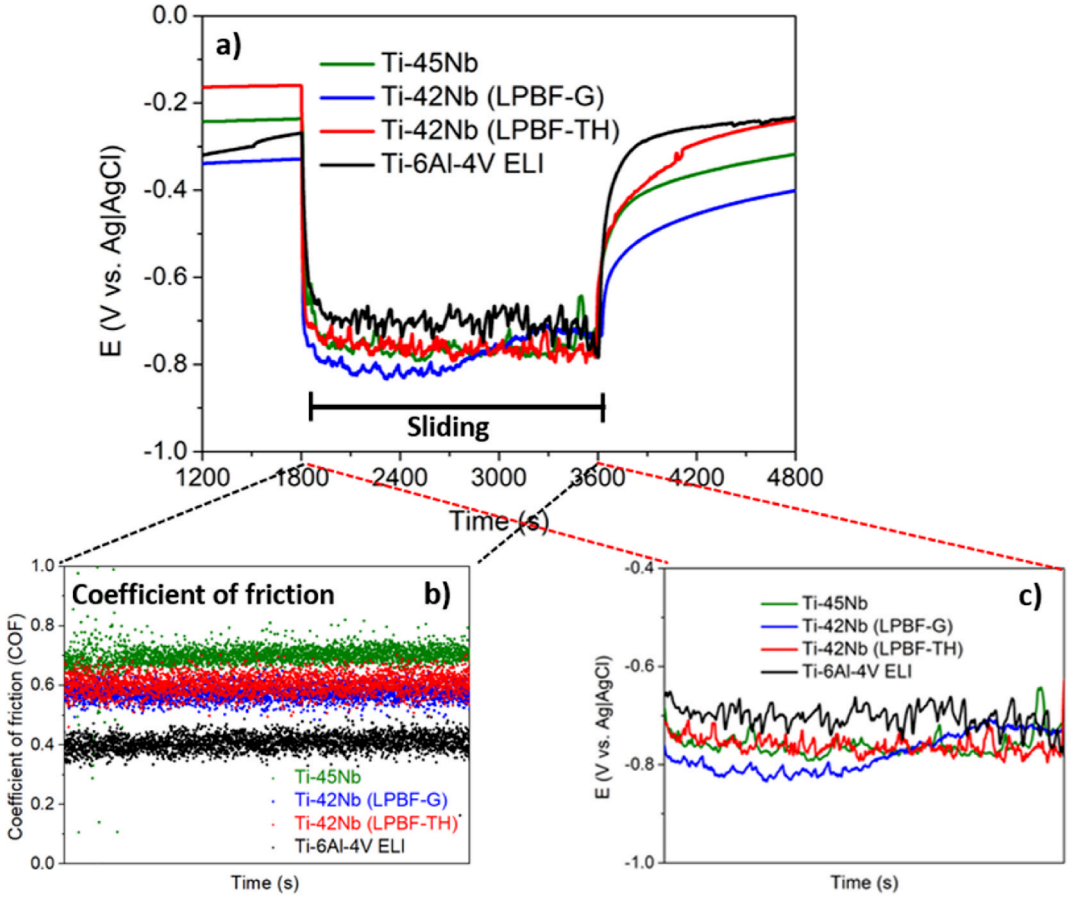


**Fig. 5.** Tribocorrosion analysis: a) Open circuit potential (OCP) evolution of Ti–45Nb, Ti–42Nb (LPBF-Gaussian laser), Ti–42Nb (LPBF-top hat laser), and Ti–6Al–4V ELI alloys in PBS solution b) Evolution of the coefficient of friction (COF) values during sliding c) Evolution of the OCP during sliding (1800 s–3600 s).

where $\Delta E$ is the potential variation (between 3600 s and 3900 s), $t$ is the certain period after sliding (usually 300 s after sliding) [72], $k_1$ is the repassivation rate of the passive film after sliding, and $k_2$ is a constant defined by the solution, which is 0.1 for PBS [72,73]. The repassivation rates ($k_1$) are calculated as: 0.10 ± 0.02, 0.08 ± 0.04, 0.11 ± 0.03, and 0.13 ± 0.03, respectively for Ti–45Nb, Gaussian, top hat, and Ti–6Al–4V ELI alloys. No significant difference was found between the repassivation rates of the studied alloy samples, which means the repassivation ability of the passive film for LPBF-produced alloys is comparable with commercial Ti–45Nb and Ti–6Al–4V ELI.

### 3.4. Analysis of worn surfaces and friction

The worn surfaces were examined with SEM and 3D profilometry to study their morphology and determine the wear mechanisms. SEM images of worn surfaces together with 3D profilometry results are shown in Fig. 6.

The worn areas indicated that wear was dominated by abrasive and adhesive wear mechanisms. The worn surfaces of the studied alloys exhibited typical features for Ti alloys, namely grooves and oxide patches (wear debris) [74–76]. In addition, for Ti alloys, adhesive wear is a common degradation mechanism on metal/ceramic sliding contacts [74]. During sliding, due to the repetitive transfers of the studied alloy between the sliding surfaces (i.e., Ti alloys and alumina pin) oxidized wear debris (yellow arrows in Fig. 6e–h) formed in the wear tracks. The oxidized debris can act as an abrasive layer on the surfaces in contact, resulting in the formation of grooves [50,74–77].

The grooves (blue arrows in Fig. 6e–h) are much shallower and narrower with superficial scratches for Ti–6Al–4V ELI alloy. The grooves are wider and deeper for LPBF-produced Ti–42Nb alloys compared to Ti–6Al–4V ELI, while the deepest grooves, with a rougher appearance, belong to Ti–45Nb. Among LPBF-produced specimens, the worn surface morphology is similar, and relatively smooth grooves (compared to Ti–45Nb) aligned parallel to the sliding direction (due to abrasion). In order to quantify the tribological parameters, total volume loss ($V_{tot}$), wear depth ($D$), and wear area were calculated from the profilometry measurements, as reported in Table 5. The results indicated that Ti–6Al–4V ELI suffered smaller material removal (with the lowest volume loss and lowest wear depth), while Ti–45Nb exhibited more severe wear with the highest volume loss and wear depth. However, LPBF-produced alloys exhibited smaller wear losses with higher wear resistance compared to Ti–45Nb. In addition, the total wear area of the worn areas well correlates with the total volume loss and wear depth results.

**Table 5**
Total volume loss ($V_{tot}$), depth of the wear track (D), and wear area determined from 3D optical profilometry, and the coefficient of friction (COF) recorded during sliding for Ti–45Nb, Ti–42Nb (LPBF-Gaussian laser), Ti–42Nb (LPBF-top hat laser), and Ti–6Al–4V ELI alloys.

| | COF | Wear depth $D$ (μm) | Total volume loss $V_{tot}$ x $10^{-3}$ ($mm^3$) | Wear area ($mm^2$) |
|---|---|---|---|---|
| **Ti–45Nb** | 0.75 ± 0.09 | 7.09 ± 0.45 | 13.19 ± 0.19 | 1.86 ± 0.09 |
| **Ti–42Nb (LPBF-G)** | 0.64 ± 0.09 | 3.89 ± 0.52 | 4.41 ± 0.42 | 1.14 ± 0.04 |
| **Ti–42Nb (LPBF-TH)** | 0.67 ± 0.05 | 4.98 ± 0.14 | 7.86 ± 0.80 | 1.58 ± 0.16 |
| **Ti–6Al–4V ELI** | 0.43 ± 0.04 | 2.67 ± 0.24 | 2.64 ± 0.36 | 0.98 ± 0.04 |

In addition, the evolution of the coefficient of friction (COF) during sliding for the studied alloys in PBS solution was also recorded (Table 5), and representative curves are shown in Fig. 5b. The COF values for the studied alloys are in line with the total volume loss and average wear depth values (the higher the COF, the higher the total volume loss). The COF values for LPBF-produced alloys are similar (0.64 and 0.67 for Gaussian and top hat lasers, respectively) and lower than Ti–45Nb (0.75). In addition, the lowest COF values belong to Ti–6Al–4V ELI (0.43).

### 3.5. Metal ion release after tribocorrosion

The metal ion content was measured from the electrolyte used for tribocorrosion tests under OCP conditions for LPBF-produced Ti–42Nb alloys. The concentration of Ti was 0.17 ± 0.16 ppb and 2.52 ± 1.77 ppb for Gaussian and top hat laser, respectively. The Nb concentration was 0.01 ± 0.02 ppb and 0.34 ± 0.25 ppb for Gaussian and top hat laser, respectively. Concentrations of Ti and Nb were within the cytotoxicity limits as reported before [78].

## 4. Discussion

β-type Ti–Nb alloys have received special attention for implant applications due to their good corrosion resistance and mechanical bio-

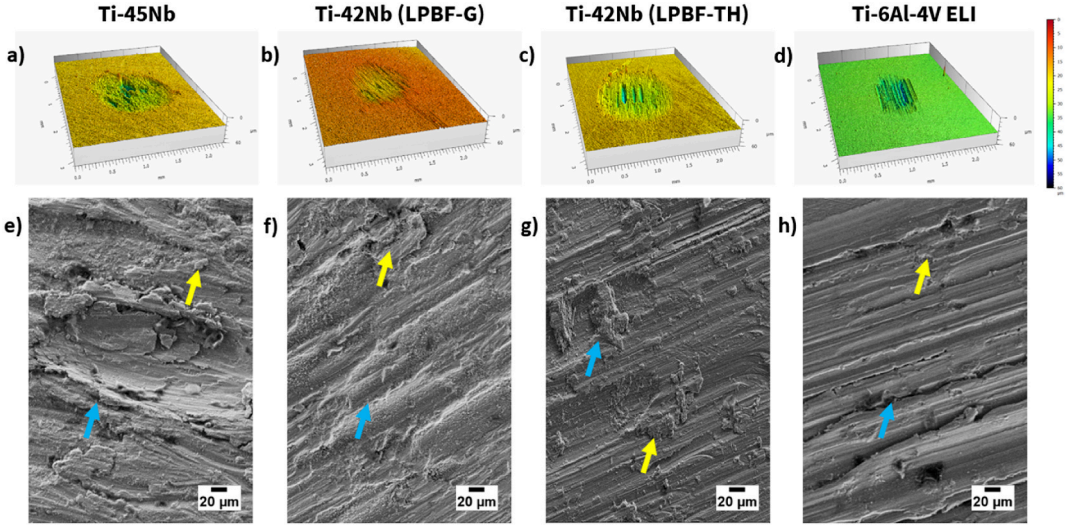


**Fig. 6.** Wear tracks of Ti–45Nb, Ti–42Nb (LPBF-Gaussian laser), Ti–42Nb (LPBF-top hat laser), and Ti–6Al–4V ELI alloys under OCP conditions characterized by (a–d) 3D optical profilometry and (e–h) SEM. Blue arrows represent the grooves, while yellow arrows indicate the wear debris. (For interpretation of the references to colour in this figure legend, the reader is referred to the Web version of this article.)

functionality [7,12,17,58]. However, load-bearing biomedical implants suffer from tribocorrosion since they are subjected to relative movements in body fluids [77]. In the present work, tribocorrosion behaviour of laser powder bed fusion (LPBF) produced β-type Ti–42Nb alloy (surfaces perpendicular to the building direction (BD)) was studied under OCP conditions and compared with that of commercially produced β-type Ti–45Nb and α+β-type Ti–6Al–4V ELI.

Two series of Ti–42Nb samples were fabricated using the LPBF process, utilizing a Gaussian and a top hat laser source with a single β-phase microstructure with promising mechanical properties, e.g. tensile strength and Young's modulus values [30,31]. The alloy samples produced with a Gaussian laser exhibit a square grain morphology perpendicular to BD with isotropic mechanical properties. However, the top hat laser configuration yield exhibits highly elongated large grains and a strong {001} texture parallel to BD leading to anisotropic mechanical properties [30]. Meanwhile, hardness values of LPBF-produced alloys are measured to be 226 $HV_{0.1}$ (Gaussian) and 230 $HV_{0.1}$ (top hat), which are higher than the microhardness of Ti–45Nb reference alloy (155 $HV_{0.1}$). This is attributed to high cooling rates and the strengthening effect of high oxygen content [54,55] on LPBF alloys. In addition, the solidification rates for the alloys produced with Gaussian laser are higher than the top hat ones.

In terms of corrosion response in PBS solution, the studied alloys exhibit low corrosion current densities (in the range of 0.22 ÷ 0.53 μA/cm$^2$) due to the spontaneous formation of protective passive films. In addition, corresponding metal ion release rates were found to be low for Ti and Nb species (within the cytotoxicity limits). However, anodic passive current densities are lower for LPBF-produced Ti–42Nb alloys (8.5 and 8.9 μA/cm$^2$ for Gaussian and top hat lasers, respectively) than for Ti–45Nb (15.5 μA/cm$^2$), which is indicative of the more protective nature of the passive films formed on LPBF-processed alloys. In addition, EIS results under OCP conditions revealed that the electrochemical response of the passive films is better for LPBF-produced alloys than Ti–45Nb. This is attributed to the formation of more adhered and less reactive oxides grown under free corrosion conditions for LPBF-produced alloys.

In terms of overall corrosion response in PBS (potentiodynamic polarization and EIS), no significant difference was found between the two LPBF-produced Ti–42Nb alloy states. This indicates that the chemical alloy composition with two strongly passivating valve metal constituents (passivation nature due to the formation of Ti–Nb mixed oxides) [58] and their homogeneous mixture in a single-phase solid solution state is more decisive than other microstructural particularities.

Generally, to generate a wear loss, many mechanisms take place under tribocorrosion conditions. Inside the wear track, wear-accelerated corrosion ($V_{wac}$) and mechanical wear ($V_{mech}$) are the responsible mechanisms for wear loss, outside of the wear track, corrosion ($V_{corr}$) is the only mechanism to generate volume loss. However, due to the strong passivation nature of Ti alloys, $V_{corr}$ can be neglected, and the overall material loss ($V_{tot}$) can be expressed according to the following relationship [79,80]:

$$V_{tot} = V_{wac} + V_{mech} \quad (2)$$

Mischler et al. [80] investigated the formation of passive films on tribocorrosion behavior of carbon steel, and results showed that the total volume loss under anodic potentiostatic polarization (in a passive state) resulted in the combined effect of electrochemical corrosion and mechanical wear, while the volume loss under cathodic potentiostatic polarization conditions is mainly attributed to mechanical wear. In our case (for all studied alloy states), the total wear loss under OCP conditions is mainly ascribed to mechanical wear, and the contribution of wear-accelerated corrosion is negligible due to the promising passivation kinetics of Ti alloys [50]. Passive films with high surface reactivity can depassivate easily under mechanical loads and the repassivation process takes longer compared to passive films with less reactivity. Due to the retardation in passivation kinetics, the wear-accelerated corrosion process might accelerate under mechanical loads [81,82]. However, in our case, mechanical wear is more decisive for tribocorrosion properties. In addition, similar observations were made for the tribocorrosion response of Ti–30Nb and Ti–30Nb–Sn (2, 4 wt% Sn) alloys (produced via powder metallurgy) against an alumina ball in PBS solution under OCP conditions [79].

According to Archard's law, the total volume loss due to the wear is inversely proportional to the hardness of the worn material [83]. The results of this study are in accordance with Archard's law as illustrated in Fig. 7. The lowest wear loss (the shallowest wear depth) is observed for the Ti–6Al–4V ELI (348 $HV_{0.1}$), while Ti–45Nb exhibits (155 $HV_{0.1}$) the highest volume loss (the deepest wear depth) under OCP conditions. On the other hand, LPBF-produced Ti–42Nb alloys exhibit similar hardness values (226 $HV_{0.1}$ and 230 $HV_{0.1}$ for Gaussian and top hat lasers, respectively). However, the alloys produced with the top hat laser configuration exhibit slightly higher volume loss than the alloys produced with the Gaussian laser. This could be attributed to the formation of compressive residual stresses that are generated during the LPBF process [47]. The alloys produced with Gaussian laser might experience higher compressive residual stresses due to the rapid cooling rates compared to the top hat ones. Thus, the formation of compressive residual stresses might offer greater wear resistance to the alloys processed with Gaussian laser configuration. However, the origin of the residual stress difference is not clear, but other researchers observed that residual stresses play a critical role [47,84]. In the end, higher hardness and wear resistance values were obtained for both LPBF-produced Ti–42Nb alloy states compared to Ti–45Nb from conventional production methods. This is mainly due to different cooling conditions and oxygen contents that lead to significantly different microstructures, as discussed above.

The lowest COF values are observed for the Ti–6Al–4V ELI (0.43), while Ti–45Nb exhibits (0.75) the highest COF, during sliding under OCP conditions. The LPBF-produced alloys exhibit similar COF values (0.64 and 0.67 for Gaussian and top hat laser, respectively). The obtained COF values in this work are comparable with the literature. Çaha et al. [75] studied the tribocorrosion response of conventionally produced Ti–40Nb alloy and compared it with the commercial Ti–6Al–4V in saline (9 g/L NaCl) electrolyte under an applied load of 1 N. They observed relatively stable (during sliding) COF values of 0.38 and 0.69 for Ti–6Al–4V and Ti–40Nb, respectively. Pina et al. [79] investigated the tribocorrosion behaviour of Ti–30Nb-xSn alloys (produced via powder metallurgy) against an alumina ball in PBS and observed COF values in the range of 0.59 ÷ 0.71.

The analysis of the worn surfaces indicated that wear loss during sliding was dominated by abrasive and adhesive wear. The accumulation of dislocations, due to plastic deformation in the sub-surface caused by the sliding against the alumina pin, may lead to the formation of cracks and voids, and these cracks may act as an initiator for more void formation under plastic deformation. When such cracks reach the surface, the delamination wear mechanism takes place due to the release of laminar wear particles. Thus, in addition to abrasive and adhesive wear,

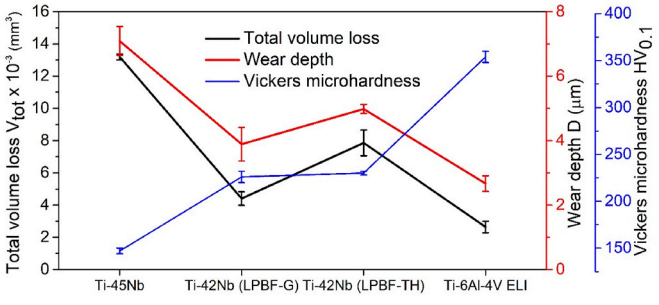


**Fig. 7.** Summary of total volume loss, wear depth, and Vickers microhardness values of Ti–45Nb, Ti–42Nb (LPBF-Gaussian laser), Ti–42Nb (LPBF-top hat laser), and Ti–6Al–4V ELI alloys.

delamination wear might play a role as a wear mechanism for the studied alloys [85–87].

LPBF-produced Ti–42Nb alloys with promising corrosion and tribocorrosion performance can be an optimistic alternative to Ti–6Al–4V. However, there is a need for further studies for real clinical applications, such as tribo-electrochemical tests in complex electrolytes (including organic molecules and salts) at body temperature under specific applied loads.

## 5. Conclusions

In this work, the corrosion and tribocorrosion performance of LPBF-produced β-type Ti–42Nb alloys (surfaces perpendicular to BD) was studied in PBS and compared with conventionally produced β-type Ti–45Nb and α+β-type Ti–6Al–4V ELI.

- β-type Ti–42Nb alloy samples were fabricated by LPBF using conventional Gaussian and high-power top hat laser configurations. The samples produced with a Gaussian laser exhibit square grains perpendicular to BD with isotropic mechanical properties. However, the top hat laser configuration generates highly elongated grains with {001} texture along BD leading to anisotropic mechanical properties.
- The overall corrosion response of the two LPBF-produced Ti–42Nb alloy states in PBS is similar to that of conventional Ti–45Nb. However, LPBF-produced alloys exhibit less reactive surfaces with better passive film properties due to the strong passivation nature of LPBF-produced alloys. However, Ti–6Al–4V ELI exhibits better passive film properties than LPBF-processed alloys.
- Under sliding conditions, all Ti alloys exhibit similar tribocorrosion mechanisms in PBS under OCP conditions, i.e. mixed abrasive wear, and adhesive wear. For LPBF-produced Ti–42Nb alloy states, the total volume loss is lower than commercial Ti–45Nb. These differences are associated with the hardness of the studied alloys (Archard's law) and the total volume loss under OCP conditions is mainly attributed to mechanical wear. However, Ti–6Al–4V ELI exhibits better tribocorrosion performance compared to LPBF-produced alloys, attributed to increased microhardness.
- In terms of overall corrosion response in PBS, no significant difference was found between the two LPBF-produced Ti–42Nb alloy states. This indicates the passivation nature of the LPBF alloys is more decisive than the microstructural particularities.
- LPBF-produced Ti–42Nb alloys exhibit similar microhardness values. However, the alloys produced with the Gaussian laser exhibit slightly lower volume loss than the top hat ones. This could be attributed to the formation of compressive residual stresses to offer greater wear resistance.

In conclusion, both LPBF-produced Ti–42Nb alloy states exhibit better tribocorrosion behaviour compared to conventionally manufactured Ti–45Nb, which is attributed to higher microhardness. LPBF-produced alloys with promising corrosion and tribocorrosion performance can be a potential candidate for load-bearing implant applications.

## Funding information

A.A., Y.D., and L.A.A. are grateful for the financial support from the European Commission within the H2020-MSCA grant agreement No. 861046 (BIOREMIA-ETN). S.P. and A.G. acknowledge funding by the Deutsche Forschungsgemeinschaft (DFG) under projects GE/1106/12 1&2 no 41995231. We acknowledge DESY (Hamburg, Germany), a member of the Helmholtz Association HGF, for the provision of experimental facilities. Parts of this research were carried out at PETRA III, and we would like to thank Emad Maawad for assistance in using beamline P07. Beamtime was allocated for proposal I-20220421.

## Declaration of competing interest

The authors declare that they have no known competing financial interests or personal relationships that could have appeared to influence the work reported in this paper.

## Acknowledgements

The authors are grateful to Bernard Normand (INSA Lyon) and Nicolas Mary (INSA Lyon) for fruitful scientific discussions. Yosra Chrigui (INSA Lyon) is acknowledged for assistance during tribocorrosion experiments. Andrea Voβ is acknowledged for the chemical analysis of the alloys.

## Appendix A. Supplementary data

Supplementary data to this article can be found online at https://doi.org/10.1016/j.jmrt.2024.06.172.

## References

[1] Miura K, Yamada N, Hanada S, Jung TK, Itoi E. The bone tissue compatibility of a new Ti-Nb-Sn alloy with a low Young's modulus. Acta Biomater 2011;7:2320–6.
[2] Ridzwan MIZ, Shuib S, Hassan AY, Shokri AA, Mohammad Ibrahim MN. Problem of stress shielding and improvement to the hip implant designs: a review. J Med Sci 2007;7:460–7.
[3] Runa MJ, Mathew MT, Rocha LA. Tribocorrosion response of the Ti6Al4V alloys commonly used in femoral stems. Tribol Int 2013;68:85–93.
[4] Gomes CC, et al. Assessment of the genetic risks of a metallic alloy used in medical implants. Genet Mol Biol 2011;34:116–21.
[5] Monteiro E, dos S, et al. Comparison of the wettability and corrosion resistance of two biomedical Ti alloys free of toxic elements with those of the commercial ASTM F136 (Ti–6Al–4V) alloy. J Mater Res Technol 2020;9:16329–38.
[6] Bai Y, et al. Characterization, corrosion behavior, cellular response and in vivo bone tissue compatibility of titanium-niobium alloy with low Young's modulus. Mater Sci Eng C 2016;59:565–76.
[7] Calin M, et al. Elastic softening of β-type Ti-Nb alloys by indium (In) additions. J Mech Behav Biomed Mater 2014;39:162–74.
[8] Helth A, et al. Effect of thermomechanical processing on the mechanical biofunctionality of a low modulus Ti-40Nb alloy. J Mech Behav Biomed Mater 2017;65:137–50.
[9] Alberta LA, et al. Effects of Ga on the structural, mechanical and electronic properties of β-Ti-45Nb alloy by experiments and ab initio calculations. J Mech Behav Biomed Mater 2023;140:105728.
[10] Pilz S, Hariharan A, Günther F, Zimmermann M, Gebert A. Influence of isothermal omega precipitation aging on deformation mechanisms and mechanical properties of a β-type Ti-Nb alloy. J Alloys Compd 2023;930:167309.
[11] Pilz S, et al. Thermomechanical processing of In-containing β-type Ti-Nb alloys. J Mech Behav Biomed Mater 2018;79:283–91.
[12] Gebert A, et al. Oxidation treatments of beta-type Ti-40Nb for biomedical use. Surf. Coatings Technol. 2016;302:88–99.
[13] Gebert A, et al. Effect of indium (In) on corrosion and passivity of a beta-type Ti-Nb alloy in Ringer's solution. Appl Surf Sci 2015;335:213–22.
[14] Helth A, et al. Chemical nanoroughening of Ti40Nb surfaces and its effect on human mesenchymal stromal cell response. J Biomed Mater Res - Part B Appl Biomater 2014;102:31–41.
[15] Alberta LA, et al. Novel low modulus beta-type Ti-Nb alloys by gallium and copper minor additions for antibacterial implant applications. J Mater Res Technol 2022;20:3306–22.
[16] Kauschke V, et al. Effects of new beta-type Ti-40Nb implant materials, brain-derived neurotrophic factor, acetylcholine and nicotine on human mesenchymal stem cells of osteoporotic and non osteoporotic donors. PLoS One 2018;13:1–18.
[17] Pilz S, et al. Metal release and cell biological compatibility of beta-type Ti-40Nb containing indium. J Biomed Mater Res - Part B Appl Biomater 2018;106:1686–97.
[18] Spears TG, Gold SA. In-process sensing in selective laser melting (SLM) additive manufacturing. Integr. Mater. Manuf. Innov. 2016;5:16–40.
[19] Awad A, Fina F, Goyanes A, Gaisford S, Basit AW. Advances in powder bed fusion 3D printing in drug delivery and healthcare. Adv Drug Deliv Rev 2021;174:406–24.
[20] Liu H, Huang X, Huang S, Qiao L, Yan Y. Anisotropy of wear and tribocorrosion properties of L-PBF Ti6Al4V. J Mater Res Technol 2023;25:2690–701.
[21] Chen LY, Liang SX, Liu Y, Zhang LC. Additive manufacturing of metallic lattice structures: unconstrained design, accurate fabrication, fascinated performances, and challenges. Mater Sci Eng R Rep 2021;146:100648.
[22] Zadeh JM, Yeganeh M, Zaree SRA, Khorasanian M. Microstructure and corrosion behavior of Ti-10Cu fabricated by selective laser melting. Mater Today Commun 2024;39:109103.
[23] Hao YL, Li SJ, Yang R. Biomedical titanium alloys and their additive manufacturing. Rare Met 2016;35:661–71.

[24] Chen LY, Cui YW, Zhang LC. Recent development in beta titanium alloys for biomedical applications. Metals 2020;10:1–29.
[25] Todai M, et al. Fabrication of the beta-titanium alloy rods from a mixture of pure metallic element powders via selected laser melting. Mater Sci Forum 2018;941 (MSF):1260–3.
[26] Fischer M, Joguet D, Robin G, Peltier L, Laheurte P. In situ elaboration of a binary Ti-26Nb alloy by selective laser melting of elemental titanium and niobium mixed powders. Mater Sci Eng C 2016;62:852–9.
[27] Schwab H, Prashanth KG, Löber L, Kühn U, Eckert J. Selective laser melting of Ti-45Nb alloy. Metals 2015;5:686–94.
[28] Zhao D, Han C, Li J, Liu J, Wei Q. In situ fabrication of a titanium-niobium alloy with tailored microstructures, enhanced mechanical properties and biocompatibility by using selective laser melting. Mater Sci Eng C 2020;111: 110784.
[29] Schulze C, Weinmann M, Schweigel C, Keßler O, Bader R. Mechanical properties of a newly additive manufactured implant material based on Ti-42Nb. Materials 2018;11:13–6.
[30] Pilz S, et al. Controlling the Young's modulus of a ß-type Ti-Nb alloy via strong texturing by LPBF. Mater Des 2022;216:110516.
[31] Pilz S, et al. Tailoring microstructure and mechanical properties of an LPBF-processed beta Ti-Nb alloy through post-heat treatments. Mater Des 2024;239.
[32] Marattukalam JJ, et al. The effect of laser scanning strategies on texture, mechanical properties, and site-specific grain orientation in selective laser melted 316L SS. Mater Des 2020;193.
[33] Nagase T, Hori T, Todai M, Sun SH, Nakano T. Additive manufacturing of dense components in beta-titanium alloys with crystallographic texture from a mixture of pure metallic element powders. Mater Des 2019;173:107771.
[34] Ishimoto T, Hagihara K, Hisamoto K, Sun SH, Nakano T. Crystallographic texture control of beta-type Ti–15Mo–5Zr–3Al alloy by selective laser melting for the development of novel implants with a biocompatible low Young's modulus. Scripta Mater 2017;132:34–8.
[35] Sow MC, et al. Influence of beam diameter on laser powder bed fusion (L-PBF) process. Addit Manuf 2020;36:101532.
[36] Günther F, et al. Structure-property relationships of imperfect additively manufactured lattices based on triply periodic minimal surfaces. Mater Des 2022; 222.
[37] Lu X, et al. The effect of Cu content on corrosion, wear and tribocorrosion resistance of Ti-Mo-Cu alloy for load-bearing bone implants. Corrosion Sci 2020; 177:1–8.
[38] Hussein MA, Mohammed AS, Al-Aqeeli N. Wear characteristics of metallic biomaterials: a review. Materials 2015;8:2749–68.
[39] Revathi A, Magesh S, Balla VK, Das M, Manivasagam G. Current advances in enhancement of wear and corrosion resistance of titanium alloys – a review. Mater Technol 2016;31:696–704.
[40] Ferreira DF, et al. Synergism between mechanical wear and corrosion on tribocorrosion of a titanium alloy in a Ringer solution. J Mater Res Technol 2019;8: 1593–600.
[41] Xu W, et al. Novel porous Ti35Zr28Nb scaffolds fabricated by powder metallurgy with excellent osteointegration ability for bone-tissue engineering applications. Mater Sci Eng C 2019;105:110015.
[42] Doni Z, et al. Dry sliding and tribocorrosion behaviour of hot pressed CoCrMo biomedical alloy as compared with the cast CoCrMo and Ti6Al4V alloys. Mater Des 2013;52:47–57.
[43] Cardoso GC, Kuroda PAB, Galindo EL, Pintão CAF, Grandini CR. Tribocorrosion behavior of Ti-Nb-5Mo alloys designed for biomedical applications. Tribol Int 2024;191:1–3.
[44] Pede D, et al. Microstructure and corrosion resistance of novel β-type titanium alloys manufactured by selective laser melting. J Mater Res Technol 2022;19: 4598–612.
[45] Hariharan A, et al. Designing the microstructural constituents of an additively manufactured near β Ti alloy for an enhanced mechanical and corrosion response. Mater Des 2022;217:110618.
[46] Qin P, et al. Corrosion behavior and mechanism of selective laser melted Ti35Nb alloy produced using pre-alloyed and mixed powder in Hank's solution. Corrosion Sci 2021;189.
[47] Chakkravarthy V, et al. Comparing bio-tribocorrosion of selective laser melted Titanium-25% Niobium and conventionally manufactured Ti-6Al-4 V in inflammatory conditions. J Alloys Compd 2023;952:169852.
[48] Bachmann F, Hielscher R, Schaeben H. Texture analysis with MTEX- Free and open source software toolbox. Solid State Phenom 2010;160:63–8.
[49] Schell N, et al. The high energy materials science beamline (HEMS) at PETRA III. Mater Sci Forum 2014;772:57–61.
[50] Andrea L, et al. Tribology International Tribocorrosion behavior of β -type Ti-Nb-Ga alloys in a physiological solution. Tribol Int 2023;181:108325.
[51] Ciulli E, Betti A, Forte P. The applicability of the hertzian formulas to point contacts of spheres and spherical caps. Lubricants 2022;10.
[52] Li Z, et al. Mechanical anisotropy of laser powder bed fusion fabricated Ti-41Nb alloy using pre-alloyed powder: roles played by grain morphology and crystallographic orientation. J Alloys Compd 2022;925:166572.
[53] Roehling JD, et al. Rapid solidification in bulk Ti-Nb alloys by single-track laser melting. Jom 2018;70:1589–97.
[54] Qazi JI, Tsakiris V, Marquardt B, Rack HJ. Effect of aging treatments on the tensile properties of Ti-35Nb-7Zr-5Ta-(0.06-0.7)O alloys. J ASTM Int (JAI) 2005;2: 457–75.
[55] Nakai M, Niinomi M, Akahori T, Tsutsumi H, Ogawa M. Effect of oxygen content on microstructure and mechanical properties of biomedical Ti-29Nb-13Ta-4.6Zr alloy under solutionized and aged conditions. Mater Trans 2009;50:2716–20.
[56] Min X, et al. Effect of oxygen content on deformation mode and corrosion behavior in β-type Ti-Mo alloy. Mater Sci Eng, A 2017;684:534–41.
[57] Geng F, Niinomi M, Nakai M. Observation of yielding and strain hardening in a titanium alloy having high oxygen content. Mater Sci Eng, A 2011;528:5435–45.
[58] Akman A, et al. Effect of minor gallium addition on corrosion, passivity, and antibacterial behaviour of novel β-type Ti-Nb alloys. J Mater Res Technol 2023;25: 4110–24.
[59] Roshchina MY, et al. Corrosion behavior of an oxide nanotube-coated β-type Ti-45Nb implant alloy in a simulated inflammatory solution. Corrosion Sci 2024;227: 111767.
[60] Chen LY, et al. Corrosion behavior and characteristics of passive films of laser powder bed fusion produced Ti–6Al–4V in dynamic Hank's solution. Mater Des 2021;208:109907.
[61] Yi G, et al. Characteristics of passive films formed on as-cast Ti–6Al-4V in Hank's solution before and after transpassivation. Front. Mater. 2021;7:1–11.
[62] Martin É, Azzi M, Salishchev GA, Szpunar J. Influence of microstructure and texture on the corrosion and tribocorrosion behavior of Ti-6Al-4V. Tribol Int 2010; 43:918–24.
[63] Liu H, et al. Nb-content-dependent passivation behavior of Ti–Nb alloys for biomedical applications. J Mater Res Technol 2023;27:7882–94.
[64] Çaha I, et al. Atomic–scale investigations of passive film formation on Ti-Nb alloys. Appl Surf Sci 2023;615:156282.
[65] Chu YH, et al. Unveiling the contribution of lactic acid to the passivation behavior of Ti–6Al–4V fabricated by laser powder bed fusion in Hank's solution. Acta Metall. Sin. (English Lett. 2024;37:102–18.
[66] Hirschorn B, et al. Determination of effective capacitance and film thickness from constant-phase-element parameters. Electrochim Acta 2010;55:6218–27.
[67] Yilmaz A, et al. Effect of microstructural defects on passive layer properties of interstitial free (IF) ferritic steels in alkaline environment. Corrosion Sci 2021;182: 109271.
[68] Lohrengel MM. Thin anodic oxide layers on aluminium and other valve metals: high field regime. Mater Sci 1993;12:243–94.
[69] Guadalupe Maldonado S, et al. Mechanical and chemical mechanisms in the tribocorrosion of a Stellite type alloy. Wear 2013;308:213–21.
[70] Hacisalihoglu I, Samancioglu A, Yildiz F, Purcek G, Alsaran A. Tribocorrosion properties of different type titanium alloys in simulated body fluid. Wear 2015; 332–333:679–86.
[71] Hanawa T, Asami K, Asaoka K. Repassivation of titanium and surface oxide film regenerated in simulated bioliquid. J Biomed Mater Res 1998;40:530–8.
[72] Xu W, et al. Effect of Mo contents on corrosion and tribocorrosion behaviors of Ti-Mo alloys for orthopaedic implant application. Corrosion Sci 2020;168.
[73] Ureña J, et al. Corrosion and tribocorrosion behaviour of β-type Ti-Nb and Ti-Mo surfaces designed by diffusion treatments for biomedical applications. Corrosion Sci 2018;140:51–60.
[74] Toptan F, et al. Corrosion and tribocorrosion behaviour of Ti6Al4V produced by selective laser melting and hot pressing in comparison with the commercial alloy. J Mater Process Technol 2019;266:239–45.
[75] Çaha I, et al. Degradation behavior of Ti-Nb alloys: corrosion behavior through 21 days of immersion and tribocorrosion behavior against alumina. Corrosion Sci 2020;167:108488.
[76] Çaha I, et al. Interactions between wear and corrosion on cast and sintered Ti-12Nb alloy in comparison with the commercial Ti-6Al-4V alloy. Corrosion Sci 2020;176: 108925.
[77] Çaha I, et al. Corrosion and tribocorrosion behavior of Ti-40Nb and Ti-25Nb-5Fe alloys processed by powder metallurgy. Metall. Mater. Trans. A Phys. Metall. Mater. Sci. 2020;51:3256–67.
[78] Li Y, Wong C, Xiong J, Hodgson P, Wen C. Cytotoxicity of titanium and titanium alloying elements. J Dent Res 2010;89:493–7.
[79] Pina VG, Dalmau A, Devesa F, Amigó V, Muñoz AI. Tribocorrosion behavior of beta titanium biomedical alloys in phosphate buffer saline solution. J Mech Behav Biomed Mater 2015;46:59–68.
[80] Mischler S, Spiegel A, Landolt D. The role of passive oxide films on the degradation of steel in tribocorrosion systems. Wear 1999;225–229:1078–87.
[81] Diomidis N, Celis J, Ponthiaux P, Wenger F. A methodology for the assessment of the tribocorrosion of passivating metallic materials, vols. 53–67; 2009. https://doi.org/10.1002/ls.
[82] Diomidis N, Mischler S, More NS, Roy M. Acta Biomaterialia Tribo-electrochemical characterization of metallic biomaterials for total joint replacement. Acta Biomater 2012;8:852–9.
[83] Archard JF. Contact and rubbing of flat surfaces. J Appl Phys 1953;24:981–8.
[84] Huang L, Kinnell P, Shipway PH. Removal of heat-formed coating from a titanium alloy using high pressure waterjet: influence of machining parameters on surface texture and residual stress. J Mater Process Technol 2015;223:129–38.
[85] Suh P. N. The delamination theory of wear. Wear 1973;25:111–24.
[86] Çaha I, et al. Crystallization and additional oxide interlayers improve the tribocorrosion resistance of TiO2 nanotubular surfaces formed on Ti6Al4V. Appl Surf Sci 2023;635.
[87] Long M, Rack HJ. Subsurface deformation and microcrack formation in Ti-35Nb-8Zr-5Ta-O(x) during reciprocating sliding wear. Mater Sci Eng C 2005;25:382–8.